

Fabrication of Nanoporous Alumina Ultrafiltration Membrane with Tunable Pore Size Using Block Copolymer Templates

Chun Zhou, Tamar Segal-Peretz, Muhammed Enes Oruc, Hyo Seon Suh, Guangpeng Wu, and Paul F. Nealey*

Control over nanopore size and 3D structure is necessary to advance membrane performance in ubiquitous separation devices. Here, inorganic nanoporous membranes are fabricated by combining the assembly of cylinder-forming poly(styrene-*block*-methyl methacrylate) (PS-*b*-PMMA) block copolymer and sequential infiltration synthesis (SIS). A key advance relates to the use of PMMA majority block copolymer films and the optimization of thermal annealing temperature and substrate chemistry to achieve through-film vertical PS cylinders. The resulting morphology allows for direct fabrication of nanoporous AlO_x by selective growth of Al₂O₃ in the PMMA matrix during the SIS process, followed by polymer removal using oxygen plasma. Control over the pore diameter is achieved by varying the number of Al₂O₃ growth cycles, leading to pore size reduction from 21 to 16 nm. 3D characterization, using scanning transmission electron microscopy tomography, reveals that the AlO_x channels are continuous through the film and have a gradual increase in pore size with depth. Finally, the ultrafiltration performance of the fabricated AlO_x membrane for protein separation as a function of protein size and charge is demonstrated.

1. Introduction

Nanoporous membranes with uniform pore size have gained growing interest in the last decade since they enable separations at the micro- and nanoscale in water filtration, molecular sorting, drug delivery, and molecular sensing applications.^[1–6] The performance of nanoporous membranes or ultrafiltration (UF) membranes depends on several critical properties: high selectivity is achieved by tailoring the pore size and obtaining narrow pore distribution, while high flux can be achieved by high porosity, nontortuous pathways, and high pressure gradient across the membrane.^[4,7] Common commercial nanoporous membranes, like polymeric UF membranes, generally exhibit random structure pores, tortuous pore paths, wide pore size distribution, and are relatively thick.^[4,6] Recently, high density porous arrays of inorganic and

hybrid organic–inorganic materials were demonstrated using a variety of nanofabrication techniques such as focused ion and electron beams^[7,8] and rapid thermal annealing of nanocrystalline silicon.^[9,10] However, most of these methods are suitable for small-scale fabrication while separation processes typically require large areas. Block copolymers (BCPs), on the other hand, are easily processed from solutions and are amenable to the large-scale roll-to-roll fabrication,^[11,12] offering a simple and scalable solution for membrane fabrication.

BCPs have been widely used to generate templates and scaffolds for fabrication of nanostructured materials, as chemically dissimilar polymer chains covalently linked together self-assemble into periodic arrays of lamellar, cylindrical, spherical, and gyroid morphologies with characteristic feature sizes of 5–50 nm.^[13] To create membranes with high pore densities, cylinder-forming BCPs are typically used, and porosity is obtained either by selectively removing one block by post-assembly etching processes,^[14–16] or by using nonsolvent induced phase separation.^[17,18] Previous studies have demonstrated the ability to fabricate nanoporous membranes with well-ordered pores, narrow pore size distribution, and high pore density using self-assembled BCPs.^[2,14–16,19–22] However, tuning the pore size to create size selectivity by design is still a major challenge in the field. An additional challenge in polymeric and BCP membranes is the membranes' high fouling


C. Zhou, Prof. P. F. Nealey
Institute for Molecular Engineering
The University of Chicago
5801 South Ellis Avenue, Chicago, IL 60637, USA
E-mail: nealey@uchicago.edu

Dr. T. Segal-Peretz
Department of Chemical Engineering
Technion – Israel Institute of Technology
Haifa 32000, Israel

Dr. M. E. Oruc
Department of Chemical Engineering
Yildiz Technical University
34210 Esenler, Istanbul, Turkey

Dr. H. S. Suh, Prof. P. F. Nealey
Institute for Molecular Engineering
Material Science Division
Argonne National Laboratory
9700 S. Cass Avenue Argonne, IL 60439, USA

Dr. G. Wu
MOE Key Laboratory of Macromolecular Synthesis and Functionalization
Department of Polymer Science and Engineering
Zhejiang University
Hangzhou 310027, China

 The ORCID identification number(s) for the author(s) of this article can be found under <https://doi.org/10.1002/adfm.201701756>.

DOI: 10.1002/adfm.201701756

tendency that occurs due to the inherent hydrophobicity of polymers.^[10] On the other hand, inorganic membranes, such as anodic aluminum oxide (AAO) membranes and titanium dioxide membranes, exhibit attractive thermal, chemical, and mechanical stability, greater fouling-resistance, and often photocatalytic ability.^[10]

Recently, sequential infiltration synthesis (SIS), a technique derived from atomic layer deposition (ALD), has been developed to selectively grow inorganic species (such as ZnO, TiO₂, and Al₂O₃) in polymers that contain polar moieties, enabling inorganic nanostructure fabrication from polymer and BCP templates.^[23–27] The SIS process is based on the selective binding of gaseous organometallic precursors to polar moieties,^[28] which produces a hybrid organic-inorganic composite. Subsequent polymer removal results in inorganic nanostructures templated by the original block copolymer morphology. SIS has been demonstrated to significantly enhance etch contrast in BCP lithography, to enable fabrication of high aspect ratio inorganic nanostructure, as well as to enhance Z contrast for scanning transmission electron microscopy (STEM) imaging and tomography of BCP films.^[24,29–33]

In this work, we harness Al₂O₃ SIS to fabricate highly ordered, isoporous, AlO_x membranes with tunable pore size, templated by BCP self-assembly, and demonstrate the selectivity capabilities of this membrane through charge-based separation of similar sized proteins. Self-assembled films of cylinder-forming poly(styrene-*block*-methyl methacrylate) (PS-*b*-PMMA) with PS cylinders in PMMA matrix were used to template the AlO_x membranes. The assembly was tuned through careful control of boundary conditions to create perpendicular PS cylinders for templating nontortuous membranes. The templating of AlO_x membrane from BCP film was characterized through a combination of scanning electron microscopy (SEM), grazing incident small angle X-ray scattering (GISAXS), and scanning transmission electron microscopy (STEM) tomography, giving detailed description of the AlO_x membrane and its 3D morphology. With the additional degrees of freedom that the SIS process provides, we varied the AlO_x membrane pore diameter

between 21 and 16 nm, using a single BCP template. Finally, the thin AlO_x membrane was combined with a supporting AAO membrane to create mechanically robust hierarchical AlO_x/AAO membrane. Utilizing the pH-responsive surface charge of metal oxides, we efficiently separated similar sized proteins with both high selectivity and high flux using the hierarchical membrane.

2. Results and Discussion

The fabrication process of BCP-templated AlO_x membrane is illustrated in **Figure 1**. A silicon wafer coated with a ≈100 nm thick water-soluble sodium salt of poly(acrylic acid) (PAA-Na) layer was used as a substrate. The substrate chemistry was modified and controlled by depositing a 10 nm thick random copolymer mat with varied PS content. Cylinder-forming PS-*b*-PMMA (C2050) films ($M_n = 20.2\text{--}50.5\text{ kg mol}^{-1}$, center to center spacing $L_0 = 38.3\text{ nm}$) were self-assembled on the random copolymer mat at various thicknesses. The polymer films were floated in deionized water and were transferred onto 60 μm thick AAO membranes with average pore size of 100 nm. Al₂O₃ SIS was performed directly on the hierarchical BCP/AAO membrane, selectively growing Al₂O₃ in the PMMA domains. Finally, the membrane sample was exposed to oxygen plasma to remove polymer components, generating ultrathin highly ordered porous AlO_x membranes on AAO support.

2.1. Self-Assembly Study of Cylinder Forming PS-*b*-PMMA with PS Cylinders

For utilizing BCP films as separation membranes, it is desired to induce the assembly of perpendicular-oriented cylinders due to their high density and direct pathway through the film. While the assembly of cylinder-forming PS-*b*-PMMA with PMMA cylinders is well documented,^[34–38] less is known about

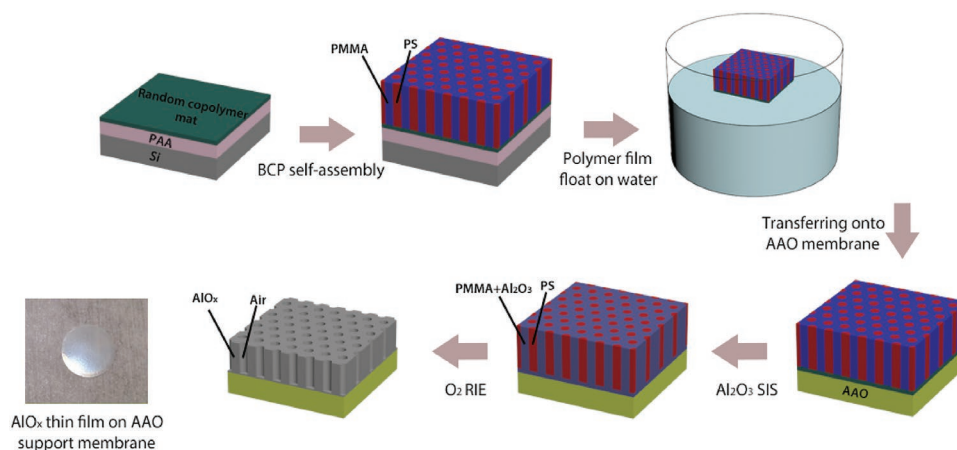


Figure 1. Schematic illustration of BCP-templated AlO_x membrane fabrication process. PS-*b*-PMMA (C2050) BCP films were self-assembled on a random copolymer mat on top of a water-soluble PAA-Na layer. The BCP and the random copolymer films were floated off in water and transferred onto AAO membranes. The polymer film was treated with Al₂O₃ SIS to selectively grow Al₂O₃ within the PMMA microdomains. After the reaction, the samples were etched by oxygen plasma to remove the polymer, resulting in nanoporous AlO_x membrane.

PS-*b*-PMMA with PS cylinders assembly. Han et al. reported nonpreferential brush and mat chemistries that can generate perpendicular-oriented PS cylinders in extremely thin **C2050** films (BCP thickness of $\approx 0.5 L_0$).^[39] However, these conditions were not sufficient to induce perpendicular orientation in films thicker than $0.5 L_0$. To rigorously study PS cylinder assembly in PS-*b*-PMMA films and to identify the thermodynamically favorable boundary conditions to achieve the desired orientation, the effects of the substrate chemistry and the annealing temperature on the domain orientation in **C2050** thin films ($\approx 0.8 L_0$) were investigated using top-down SEM imaging (**Figure 2**). Silicon wafers coated with the crosslinked polystyrene-*random*-poly(methyl methacrylate) mats with different styrene mole fractions F_{St} (ranging from 0.21 to 0.85, **21S-85S**) were used as substrates. The thermal annealing temperature, T , was varied between 190 and 270 °C, and the films were annealed for 30 min.

On F_{St} mats, **21S-63S**, the surface morphology progressed from parallel cylinders to perpendicular cylinders with increasing F_{St} , and vertical cylinders were observed when F_{St} was around 0.63. As F_{St} was increased above 0.63, the area fraction of vertically oriented structures decreased, and perpendicular cylinders formed only over small areas on **85S**. Even for films assembled on **63S**, and in particular for temperatures below 230 °C, nonperfect morphologies were observed with some bridging between adjacent cylinders, in agreement with previous work conducted at 190 °C.^[39]

Since the annealing temperature also plays an important role in modulating the domain orientation, the effect of the annealing temperature was studied. When the substrate composition induced perpendicular morphology ($0.56 \leq F_{St} \leq 0.73$), a wider perpendicular process window was observed with an increase in the annealing temperature. While at 190 °C, only at $F_{St} = 0.63$, a majority of vertically oriented structures was observed, at 270 °C, **C2050** assembled into vertically oriented structures between $0.56 \leq F_{St} \leq 0.73$. In addition, the number of parallel defects decreased when the annealing temperature was increased from 190 to 270 °C.

Self-assembly behavior of a BCP film is governed by the interfacial interactions both at the bottom and top of a film. Thus, the annealing temperature that affects the surface energy of PS and PMMA (γ_s and γ_m , respectively) is as critical as the surface chemistry of substrate to achieve the targeted BCP orientation. γ_s and γ_m become nearly equal at 250 °C, which is considered to be the optimized annealing temperature for symmetric lamella forming PS-*b*-PMMA films.^[40,41] However, in perpendicular orientation of **C2050**, larger PMMA fraction is exposed at the free surface compared with symmetric lamella forming PS-*b*-PMMA films; thus, conditions for slightly PMMA preferential free surface are desired. At 270 °C, γ_m becomes lower than γ_s , yielding a more stable free surface for this asymmetric PS-*b*-PMMA film and leading to defect-free perpendicular PS cylinders, as was seen by top-down SEM in **Figure 2** (**63S** and **73S**). For comparison, the optimized annealing temperatures for PMMA cylinders in the PS matrix (**C4621**, $M_n = 46\text{-}b\text{-}21 \text{ kg mol}^{-1}$) were reported as 210–230 °C, at which the free surface is slightly PS preferential.^[36,38] It is important to note that the annealing temperature also plays a role in the nucleation at free surface and in the pattern coarsening dynamics.^[36,42] Faster coarsening

dynamics could be an additional reason for better defined cylinders formed in the high temperature regime. As shown in **Figure 2**, optimization of annealing temperature in combination with fine turning of substrate chemistry enabled us to achieve desired perpendicular PS cylinders in the PMMA matrix.

In order to maintain the mechanical strength of BCP films and AlO_x membranes, it is desirable to use semithick block copolymer films as templates (thickness $>100 \text{ nm}$). To examine the film morphology as a function of thickness, three sets of **C2050** films with thickness ranging from 20 to 401 nm were compared and the surface morphologies of films were imaged after annealing at 270 °C for 3 h (**Figure 3**). The high temperature which was chosen to induce perpendicular morphology in **C2050** also facilitates rapid assembly of BCP films. Therefore, we assumed that the BCP films have reached close to equilibrium state in 3 h. On **63S** modified silicon substrates which were shown to be a nonpreferential substrate for **C2050** thin films (**Figure 2**), high-degree of perpendicular structures were obtained in most of the film thicknesses. Such thickness-independent orientation indicates that both the bottom and top surfaces of BCP films are nonpreferential.^[43,44] In addition, the grain size increased with the film thickness, in agreement with Ji et al.'s study on cylinder-forming PS-*b*-PMMA with PMMA cylinders (**C4621**, $M_n = 46\text{-}b\text{-}21 \text{ kg mol}^{-1}$).^[38]

On **30S** and **85S** modified substrates, different behavior was observed compared with films assembled on **63S**. In films thinner than 141 nm for **30S** and 93 nm for **85S**, the films exhibited various morphologies including hole/island, hexagonally perforated lamellae, and parallel cylinder, rather than perpendicular hexagonally packed cylinders. On the other hand, films thicker than 141 nm (on **30S**) and thicker than 93 nm (on **85S**) showed perpendicular morphology with only few parallel defects at the top surface, similar to what was observed in films assembled on **63S**.

The change in coupling between the mat chemistry and surface morphology at the various thicknesses reveals the effect of boundary conditions on surface morphology in semi-thick films. At thickness smaller than $\approx 100 \text{ nm}$, the polymer–substrate boundary condition dominates the assembly and determines the domain orientation of the block copolymer throughout the film thickness. At thicknesses above $\approx 100 \text{ nm}$, on the other hand, the polymer–substrate and polymer–free surface boundary condition are decoupled, and the polymer–free surface interaction determines the domain orientation of cylinders near the film surface regardless of the chemistry of the underlying substrate. This decoupling of boundary conditions in thick BCP films is in good agreement with previous reports on other cylinder forming BCP.^[36,38]

To utilize BCP films as templates for inorganic membranes, it is important to have perpendicular cylindrical domains through the entire film thickness that would lead to membranes with high connectivity and direct pathways. Nonpreferential boundaries are necessary but not sufficient condition to ensure through-film continued cylinders; at thick and semithick films, noncoupled nucleation occurs simultaneously at the substrate and at the free surface, which could result in noncontinuous perpendicular cylinders even when perpendicular assembly

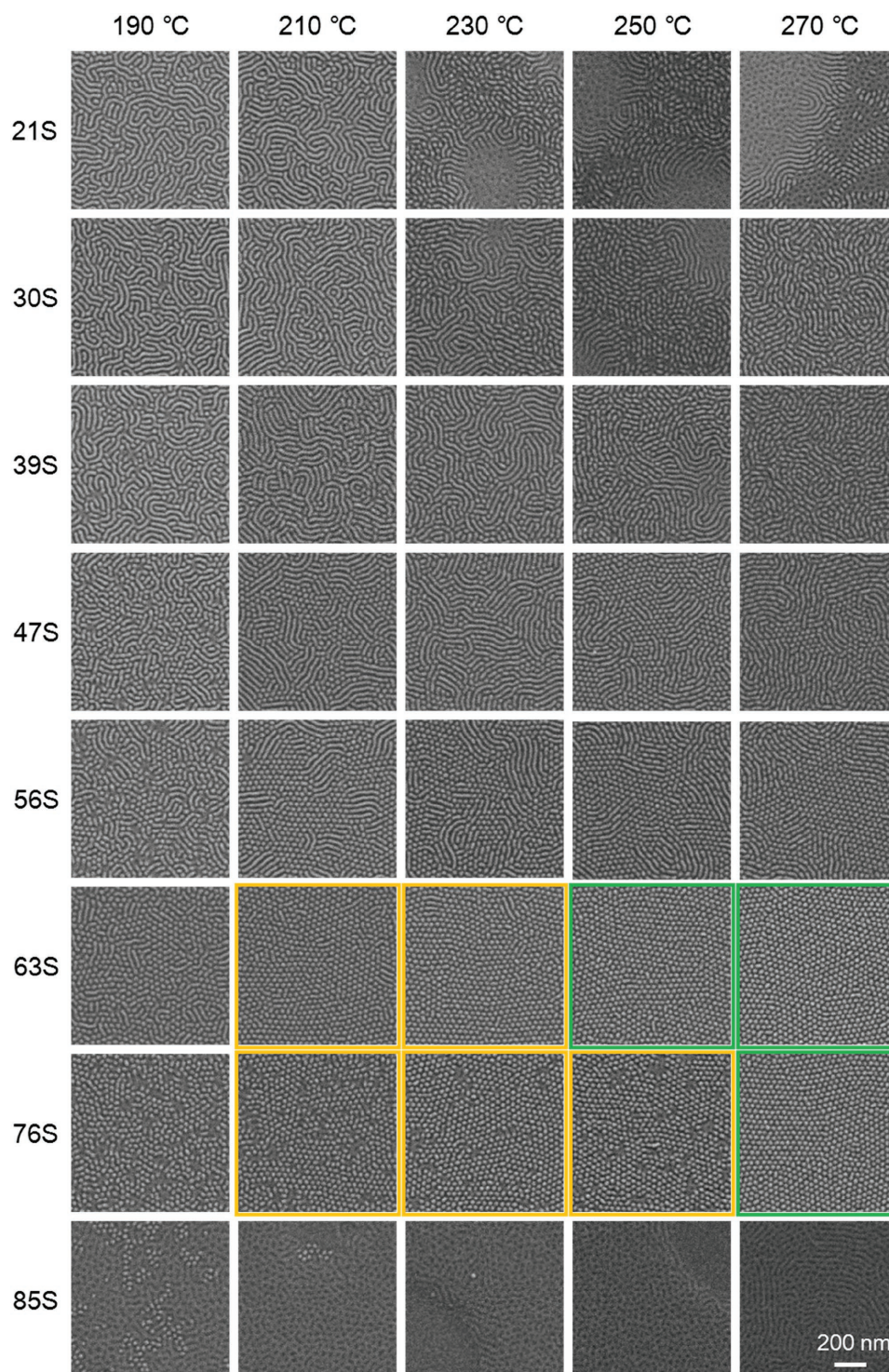


Figure 2. Top-down SEM images of 30 nm ($0.8 L_0$) thick **C2050** films on chemically modified substrates containing different mole fractions of styrene and annealed at various temperatures. Dark gray and light gray borders indicate defect-free perpendicular PS cylinders in PMMA matrix, and nearly defect-free perpendicular cylinders with few defects around grain boundaries, respectively.

occurs at both interfaces.^[36,38,42] In order to ensure continuous PS cylinders and template thin AlO_x membrane that would enable high flux, the BCP film thickness was selected to be 141 nm and **63S** was selected as the mat chemistry. The good

assembly of **C2050** film was demonstrated in lower magnification SEM image shown in Figure S1 (Supporting Information). The continuity of cylinder channels will be further discussed in Sections 2.2 and 2.3.

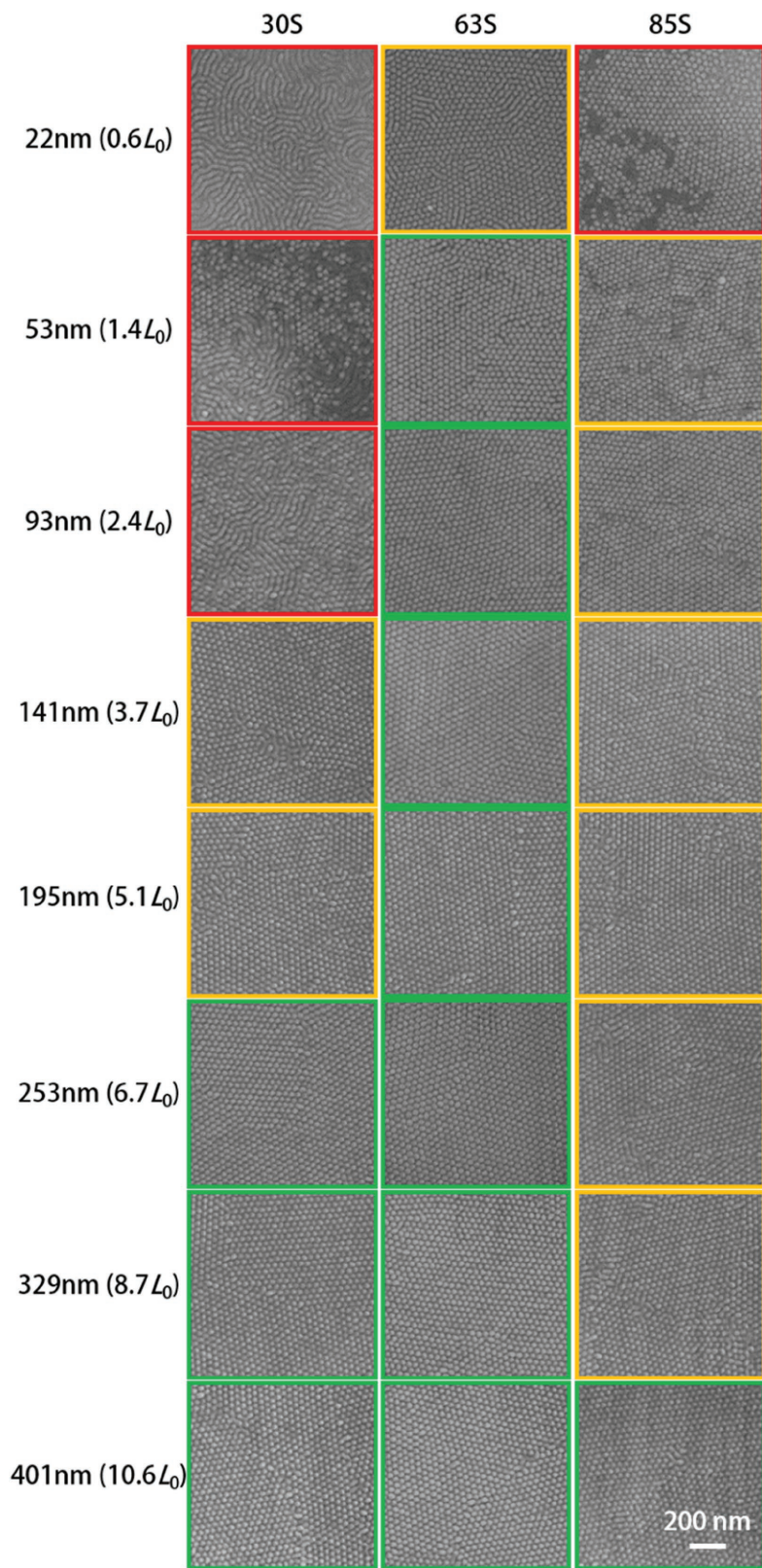


Figure 3. Top-down SEM images of C2050 films with different thickness on 30S, 63S, and 85S. Samples were annealed at 270 °C for 3 h under a nitrogen atmosphere. Green, yellow, and red colors indicate defect-free perpendicular PS cylinders in PMMA matrix, PS cylinders with defects around the grain boundaries, and other morphologies, respectively.

2.2. BCP-Templated AlO_x Membrane

To fabricate the BCP-templated AlO_x membranes, Al_2O_3 SIS was performed using multiple trimethylaluminum/water (TMA/ H_2O) exposure cycles followed by oxygen plasma to remove the polymer (see the Experimental Section for details). **Figure 4** shows the morphology of the BCP film, the hybrid BCP- Al_2O_3 nanostructure after 3 cycles of TMA/ H_2O SIS, and the nanoporous AlO_x membrane after oxygen plasma etching, using both SEM imaging (Figure 4a) and GISAXS (Figure 4b). SEM images show that the hexagonal morphology at the surface was maintained during SIS and plasma etch processes and the Al_2O_3 growth occurred primarily in the PMMA domains, in agreement with previous SIS studies.^[25,26] The AlO_x membrane showed mostly cylindrical pores with few short openings caused by merging and splitting of cylinder domains around grain boundaries, and large-scale defects were not observed (Figure S2, Supporting Information). To analyze the ordering through the entire film thickness, films were characterized by GISAXS. The incidence angle α_i between the X-ray and the film's surface was set to 0.200° , above the critical angle of the BCP. For all three samples, multiple strong vertical peaks were present only in the q_y direction, corresponding to perpendicularly oriented domains. Four intense multiple-order Bragg-rod peaks at scattering vector ratios of $q/q^* = 1 : \sqrt{3} : \sqrt{4} : \sqrt{7}$, as shown in Figure 4c, indicated hexagonal packing in all three samples, in agreement with the SEM results (Figure 4a). The average center-to-center distance in the plane of films, measured from the peak position of first four peaks, was 38.3 nm for all samples, confirming that the SIS and the etch process did not change the periodicity of lateral structures and that the AlO_x membrane was indeed templated by the BCP film. Additionally, the absence of diffuse elliptical scattering (Debye-Scherrer ring), which corresponds to tilted or randomly oriented domains,^[45,46] supports that the formation of vertically oriented cylinders is throughout the film. While the periodicity was maintained through the processes, the number of high order peaks in the GISAXS significantly differs between the samples. The hybrid BCP- Al_2O_3 had an additional high order diffraction peak compared with the pristine BCP film, while the AlO_x nanostructure had as many as ten diffraction peaks, highlighting the long-range order of the AlO_x membrane. The increase in high

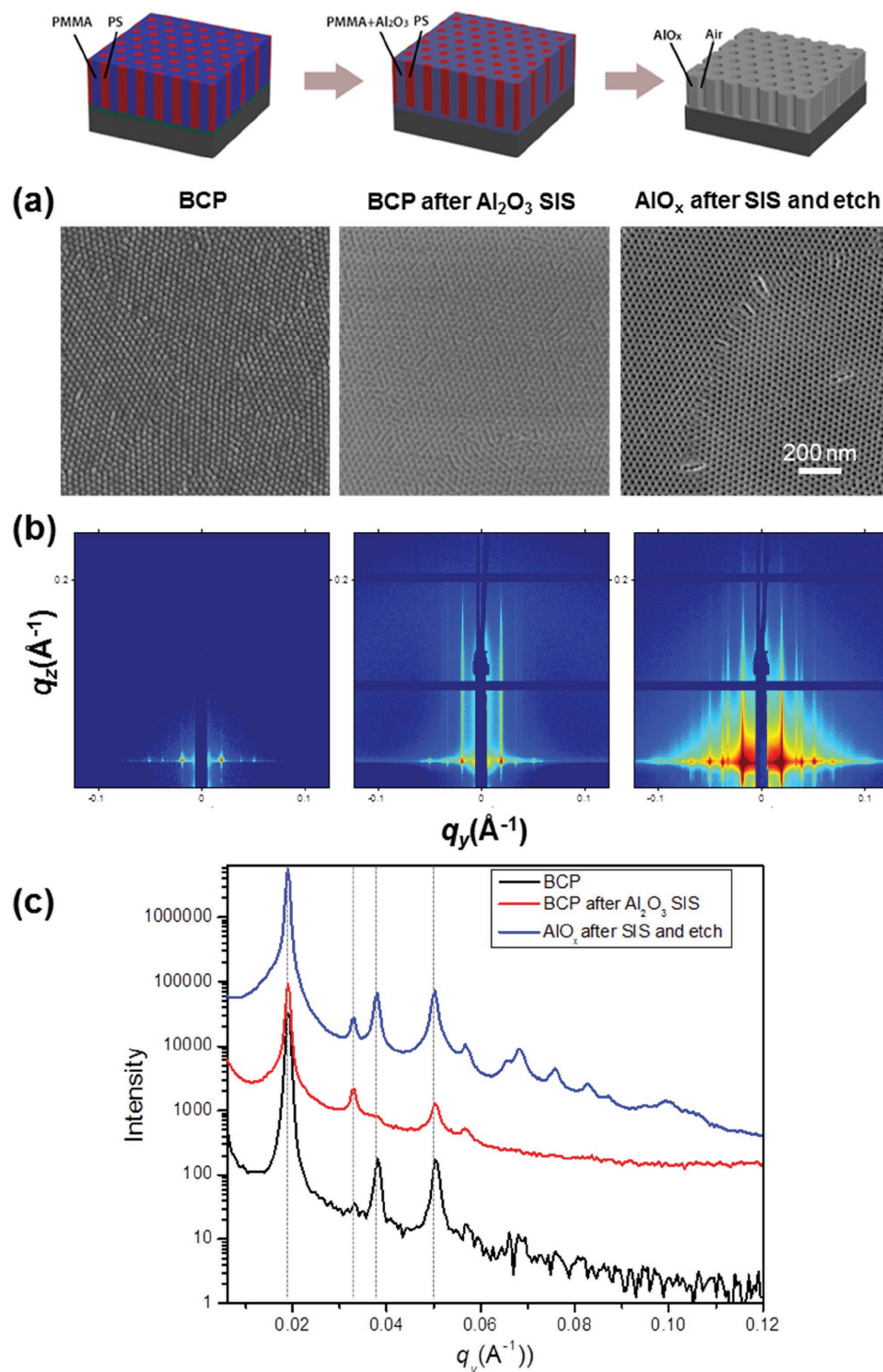


Figure 4. a) SEM images of 141 nm thick **C2050** BCP film, BCP film treated with 3 TMA/H₂O cycles of SIS, and nanoporous AlO_x structure formed after O₂ etching. b) Corresponding GISAXS scattering pattern at incident angle $\alpha_i = 0.200^\circ$. c) Line intensity scanned along the in-plane direction around Yoneda peak versus q_y .

order peaks originates from the increase in X-ray scattering contrast between PS and Al₂O₃ incorporated in PMMA domains and between AlO_x and air in the nanoporous AlO_x structure formed after the oxygen etching.

Analysis of the GISAXS data also reveals a hump in the high q range of the hybrid BCP–Al₂O₃ film scattering pattern (Figure S3, Supporting Information). This hump was not observed in the nanoporous AlO_x structure formed after oxygen

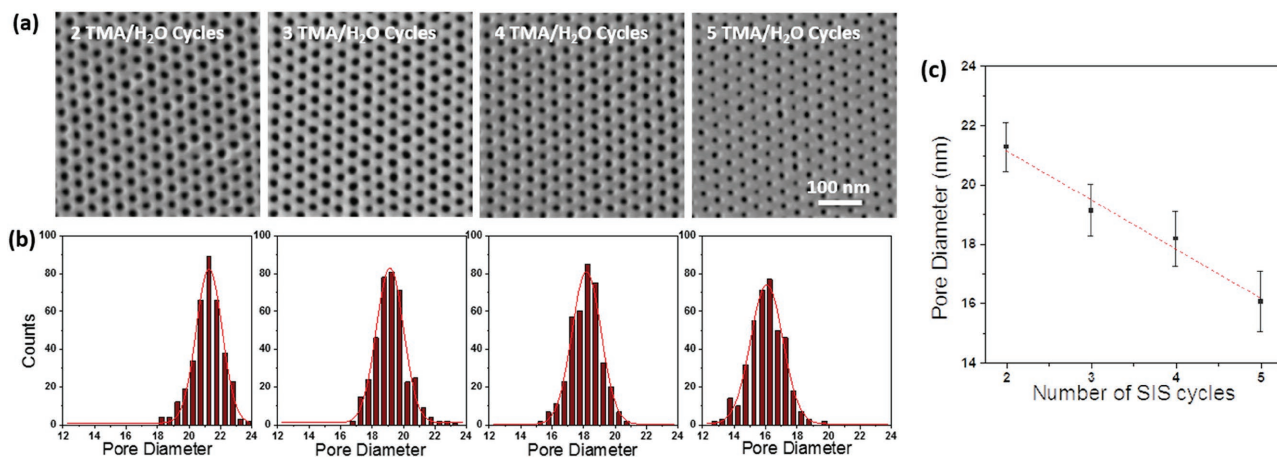


Figure 5. Pore size tuning through SIS cycles: a) SEM images of AlO_x membranes templated by 141 nm thick C2050 film using 2, 3, 4, and 5 cycles of TMA/H₂O SIS, followed by oxygen plasma etch. b) Pore size distribution calculated from ≈240 pores. c) Pore diameter as a function of cycle number.

etching. We hypothesize that the Al₂O₃ particles formed during the SIS process have weak ordering with average spacing of ≈3.5 nm, while the AlO_x in the porous membrane is closely packed. This observation is in good agreement with previous reports on the dimension shrinkage during post-SIS etch process.^[30,47] Detailed distribution of inorganic nanoparticles during SIS process is under ongoing investigation.

To investigate the pore-size tunability, 141 nm thick BCP films assembled on 63S modified substrates were treated with various number of TMA/H₂O cycles followed by oxygen plasma etching. Increasing the number of SIS cycles resulted in hexagonally packed pores with decreasing pore sizes, as shown by top-view SEM imaging (Figure 5a). The average pore diameters at the film surface were 21.3 ± 0.8, 19.1 ± 0.9, 18.2 ± 0.9, and 16.1 ± 1.0 nm when BCP films were exposed to 2, 3, 4, and 5 TMA/H₂O cycles, respectively (Figure 5b and Table 1); the corresponding open area fractions *f* are listed in Table 1. The pore size was linearly dependent on the number of SIS cycles (Figure 5c), but as the average pore diameter decreased, the pore size distribution gradually became wider.

The decrease in pore size is the result of higher Al₂O₃ content in the PMMA domain with additional cycles, which leads to thicker AlO_x matrix after oxygen etching. The Al₂O₃ growth at the surface becomes less uniform with additional cycles, as evident from the increase in standard deviation with cycles. However, since Al₂O₃ growth in SIS occurs throughout the film thickness, a more thorough inspection of the 3D structure is needed in order to fully understand the growth of Al₂O₃ with SIS cycles. By controlling the growth of Al₂O₃ in the BCP, we were able to decrease the pore size by ≈25%, demonstrating the ability to tune the pore size from a single BCP template. Further decrease in pore size can be conducted using additional SIS cycles or ALD coatings.

2.3. The 3D Structure of AlO_x Membranes

While the pore size at the membrane surface is an important factor, the membrane performance is determined by its entire 3D structure. In order to probe the 3D morphology of

the pores and verify that the cylinder channels are indeed continuous throughout the entire membrane thickness, STEM tomography^[33] was used to directly resolve the 3D structures of the membrane with high resolution. For STEM imaging, 141 nm thick BCP film assembled on 63S modified substrate was floated (together with the random copolymer layer) onto deionized water and was transferred onto a silicon nitride window,^[48] followed by Al₂O₃ SIS and O₂ etch under the same conditions previously described.

Visualization of the 3D reconstructed volume of AlO_x membrane prepared using 3 SIS cycles, obtained by angular dark field (ADF) STEM tomography, is shown in Figure 6a and Movie S1 (Supporting Information); for clarity, the AlO_x is colored in blue and the pores are transparent. To better understand the pores structure, the reconstructed volume was digitally sliced in *xy* and *yz* planes, creating slices parallel and perpendicular to the substrate, respectively. Figure 6b–d shows 0.68 nm thick *xy* slices taken at the top, middle, and bottom of the film (*z* ≈ 58 nm, *z* ≈ 34 nm, and *z* ≈ 6 nm, respectively, where *z* ≈ 0 nm is the SiN_x substrate). The bright regions in the ADF-STEM images are the strong scattering AlO_x, while the darker regions are the pores. The *xy* slices show perpendicular pores throughout the AlO_x thickness with some decrease in perpendicularity at the bottom of the membrane (Figure 6d). The tomographic characterization indicates that the original BCP film, which templated the AlO_x membrane, had perpendicular-oriented PS cylinders in the entire film thickness, in good agreement with the GISAXS characterization results (Figure 4). The perpendicularity of the pores can also be clearly seen in the cross-sectional *yz* slice (Figure 6e). The AlO_x membrane thickness, measured from the *yz* slices, was ≈62 nm; i.e., the film shrank in *z* direction by 56% during etching, similar to recent studies on ZnO, AlO_x, and TiO_x nanostructures formed by SIS in polymers.^[23]

Figure 6b–e shows that the pore size changes as a function of depth and the sidewalls become thinner at smaller *z*. To analyze the change in pore size with depth, the average pore diameter of 240 pores was measured in each *xy* slice of the tomography reconstructed volume using watershed segmentation and the pore diameter was plotted as a function of *z* (Figure 6f). Close

Table 1. Average pore diameter, standard deviation, and open area fraction of AlO_x membranes templated by 141 nm thick C2050 film using various cycles of TMA/ H_2O SIS, followed by oxygen plasma etch. The measurements were done using SEM images, 700 nm \times 700 nm in size, with \approx 240 pores.

Number of SIS cycles	Average pore diameter [nm]	Standard deviation (1σ) [nm]	Open area fraction (f)
2	21.3	0.8	0.280
3	19.1	0.9	0.226
4	18.2	0.9	0.205
5	16.1	1.0	0.160

to the surface ($z = 60$ nm), average pore size of 26.1 ± 2.4 nm was measured, with minor change in diameter until $z = 50$ nm. Below $z = 50$ nm, the pore size gradually increased toward the substrate (until $z = 20$ nm), where at the bottom of the film ($z = 8$ nm), average pore size of 32.0 ± 4.1 nm was measured. Below $z = 7$ nm, the signal to noise ratio was too low for a reliable measurement. The measured pore size at the surface from the tomography data was higher than what was measured from the SEM images; we attribute this difference to the different interaction of the specimen with the electron beam and the detecting systems in the two imaging systems.

The change in pore size through depth indicates that for the SIS conditions used in this study, more Al_2O_3 growth occurred

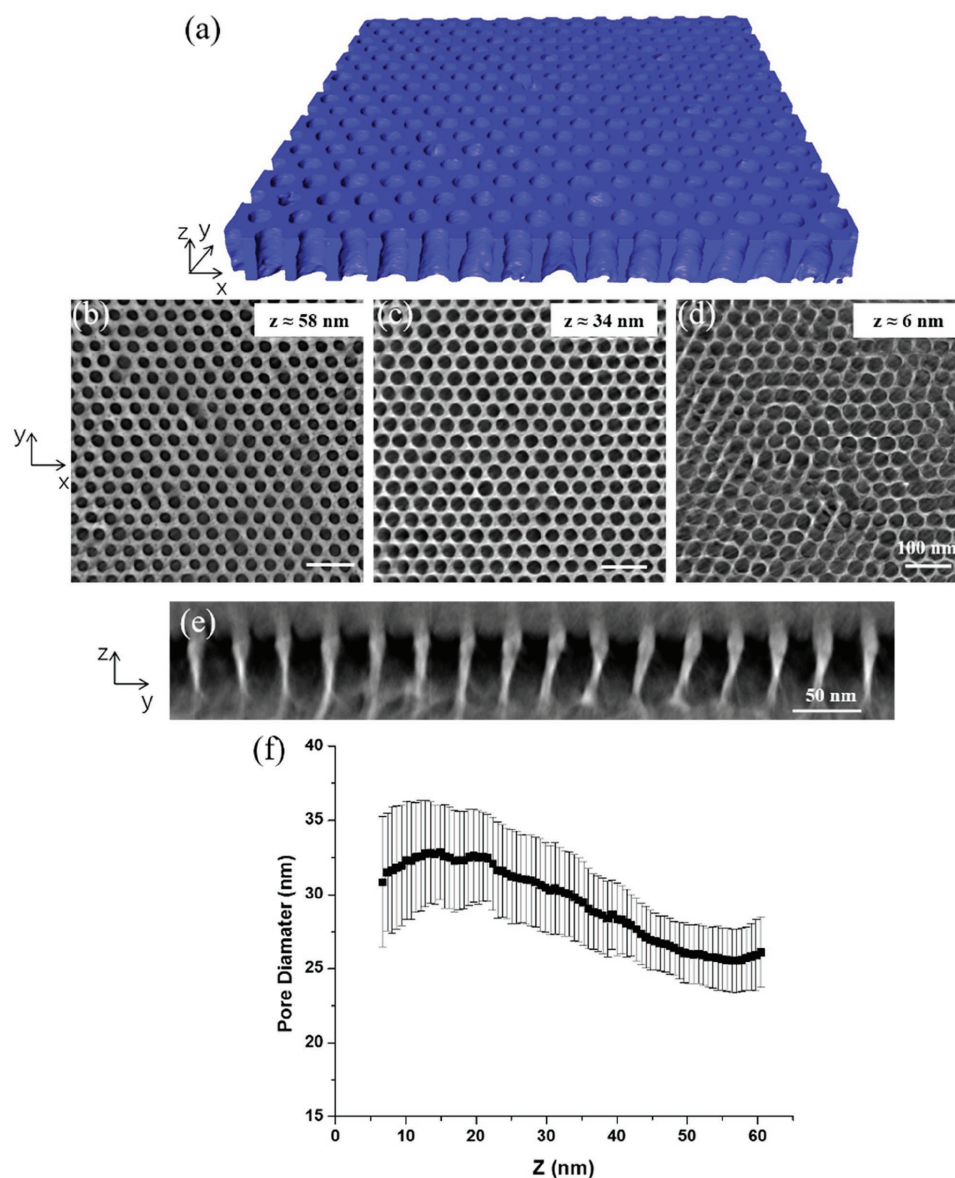


Figure 6. STEM tomography characterization of alumina membrane templated by C2050 using 3 cycles of AlO_x SIS followed by polymer etch: a) visualization of the reconstructed volume; the dimensions of the reconstructed volume are 635, 612, and 62 nm (x, y, z). b–d) 0.68 nm thick, xy slices of the reconstructed volume at z high of 6, 34, and 58 nm, respectively. $z = 0$ is defined as the height at the SiN_x substrate. e) yz digitally sliced cross-section of the reconstructed volume. f) Pore diameter as a function of depth.

at the top third of the film compared to the bottom of the film. Since SIS is a diffusion-limited process, more uniform Al_2O_3 growth could be expected if longer exposure time is used.^[49,50] Additionally, purge time could affect the SIS growth due to the unstable nature of physisorbed PMMA–TMA complex.^[50] Optimizing purge time could minimize the amount of precursor that is physically absorbed at the top of the film and allow covalent bonding to form between the metal precursor and the polymer moieties inside the film.^[50] However, for separation applications, the widening of pores with depth is desired, since the narrow pore size enables high selectivity and the widening of the pores leads to high flux.^[15,17]

2.4. Similar Sized Protein Separation

Using a U-shaped diffusion cell (Figure 7a), separation tests were conducted on alumina membranes using two similar-size proteins in buffer solutions (see the Experimental Section). Bovine serum albumin (BSA) and bovine hemoglobin (BHb) were chosen as a model system since they have similar volumes ($14 \text{ nm} \times 3.8 \text{ nm} \times 3.8 \text{ nm}$ and $6.4 \text{ nm} \times 5.5 \text{ nm} \times 5 \text{ nm}$, respectively);^[51,52] thus, their electrical charge can be tuned by varying the pH value of the buffer solution (Figure S4, Supporting Information). The ionic strength of the buffer solution was chosen to be 0.01 M since it results in Debye length of $\approx 3.3 \text{ nm}$ in the electric double layer (EDL) which is developed around the charged proteins and the charged pore walls (see the Experimental Section). This Debye length is significant for pore sizes of $\approx 20 \text{ nm}$ and proteins diameters of $\approx 6 \text{ nm}$.^[21,53,54] The flux and the separation selectivity were compared between three membranes: (a) the hierarchical AlO_x/AAO membrane developed in this study (AlO_x membrane templated by the 141 nm thick BCP film treated with 3 cycles of Al_2O_3 SIS and transferred onto a commercially available AAO membrane with 100 nm pores), (b) commercially available AAO membrane with 100 nm pores, and (c) commercially available AAO membrane with 20 nm pores.

The average flux of the proteins at $\text{pH} = 4.7$ and $\text{pH} = 7.0$ in a mixed protein diffusion experiment using these three

membranes is presented in Figure 7b. The flux values were normalized according to the open area fraction of each membrane, taking into account that 37% of AlO_x pores are blocked by the AAO membrane underneath. At $\text{pH} = 4.7$, BSA diffused through AAO membrane with average pore size of 100 nm at high flux of $(2.6 \pm 0.1) \times 10^{-9} \text{ M cm}^{-2} \text{ s}^{-1}$, and the flux of BHb was only slightly lower $((2.3 \pm 0.1) \times 10^{-9} \text{ M cm}^{-2} \text{ s}^{-1})$. These flux values are in good agreement with other protein separation results using membranes with the same characteristic pore size.^[51,54] The selectivity of separation, calculated from the flux ratio between two proteins, was 1.1 ± 0.1 (Figure 7c). Although at $\text{pH} = 4.7$ BSA has neutral charge while BHb and the AlO_x membrane are positively charged (Al_2O_3 isoelectric point is 9), the difference in the charge states has little effect on the separation selectivity since the effective pore size (with the EDL) is considerably larger than the hydrated protein diameters. The same behavior was seen at $\text{pH} = 7.0$, where both proteins showed high flux (BSA flux: $(2.1 \pm 0.1) \times 10^{-9} \text{ M cm}^{-2} \text{ s}^{-1}$, and BHb flux: $(2.2 \pm 0.1) \times 10^{-9} \text{ M cm}^{-2} \text{ s}^{-1}$), leading to low selectivity of 1.1 ± 0.1 .

When AAO membrane with average pore size of 20 nm was used for separating the two proteins, small increase in selectivity was measured (1.5 ± 0.2 and 1.3 ± 0.2 for the pH values of 4.7 and 7, respectively), but with low flux values of $(1.8 \pm 0.2) \times 10^{-10}$ – $(2.8 \pm 0.2) \times 10^{-10} \text{ M cm}^{-2} \text{ s}^{-1}$. At pore diameter of 20 nm , the effective pore size is close to the hydrated protein diameter and the proteins have to diffuse through $60 \mu\text{m}$ thick membrane, resulting in lower flux compared to the 100 nm pore AAO membrane. The relatively small increase in selectivity was attributed to the large thickness of the membrane and the wide distribution of pore sizes.^[52]

When the hierarchical membrane with 62 nm thick top layer of porous AlO_x templated by BCP (SIS membrane) was used to separate the proteins, both high flux and high selectivity were observed. At $\text{pH} = 4.7$, BSA flux was $(1.4 \pm 0.1) \times 10^{-9} \text{ M cm}^{-2} \text{ s}^{-1}$ and BHb flux was $(1.8 \pm 0.1) \times 10^{-10} \text{ M cm}^{-2} \text{ s}^{-1}$, resulting in selectivity of 7.7 ± 0.1 , while at $\text{pH} = 7.0$, BSA flux and BHb flux were $(2.6 \pm 0.1) \times 10^{-10}$ and $(1.1 \pm 0.1) \times 10^{-9} \text{ M cm}^{-2} \text{ s}^{-1}$, respectively, resulting in selectivity of 4.1 ± 0.1 . The high flux through the AlO_x membrane and the threefold to fivefold increase in selectivity compared to the 20 nm pores size AAO membrane

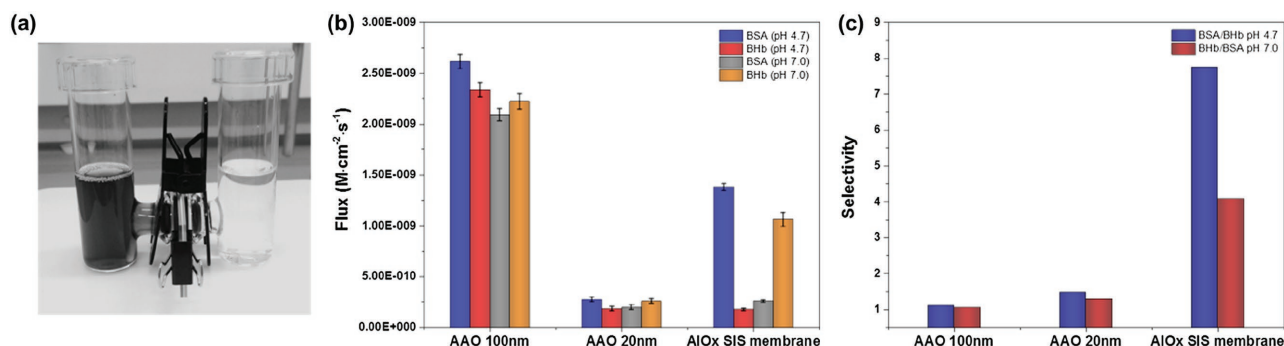


Figure 7. The separation of similar sized proteins: a) the separation performance of membranes was tested using a U-shaped cell. b) The flux of BSA and BHb measured at pH values of 4.7 and 7.0 through three different membranes: AAO membrane with average pore diameter of 100 nm , AAO membrane with average pore diameter of 20 nm , and a hierarchical membrane with BCP-templated AlO_x membrane on top of AAO membrane with average pore diameter of 100 nm (AlO_x SIS membrane). c) Separation selectivity of BSA/BHb at pH 4.7 and BHb/BSA at pH 7 for the three membrane types.

are attributed to the ultrathin selective layer (62 nm, Figure 6) and the narrow pore size distribution (19.1 ± 0.9 nm, Figure 5), that enable to effectively harness the charged protein–membrane interactions. At pH = 4.7, the positively charged BHB can barely diffuse through the positively charged membrane, while BSA, which does not carry electrical charges, can efficiently diffuse through the 60 nm thick AlO_x membrane. At pH = 7.0, BSA is negatively charged while BHB is neutral, leading to efficient diffusion of BHB through the hierarchical membrane.

The combination of hierarchical alumina membrane with thin separating layer and uniform nanoscale pores resulted in improved performance over commercial AAO membranes. Future development of this BCP-templated inorganic membrane for water UF should include a comparison between this type of membrane and commercially available polymeric UF membranes. With the progress recently demonstrated in roll-to-roll processes for both BCP^[11] and ALD^[55] and further engineering of the support layer to create low-roughness, low-cost, robust substrate, BCP-templated inorganic membrane could be fabricated on a large scale.

3. Conclusion

In summary, we have demonstrated that PMMA-rich, cylinder-forming PS-*b*-PMMA can be harnessed to template nanoporous AlO_x membranes with narrow pore size distribution and precise control over the pore size, and showed the protein separation capabilities of this membrane. Perpendicular-oriented PS cylinders were self-assembled in PMMA-rich PS-*b*-PMMA films over a large range of film thickness by precisely controlling the substrate chemistry and the annealing temperature. Nanoporous AlO_x membranes with tunable pore size were templated by the same BCP film through varying the amount of Al_2O_3 grown inside the PMMA domains in the SIS process. GISAXS and electron microscopy showed the highly ordered hexagonally packed structures of the BCP film, the hybrid intermediate, and the AlO_x nanoporous membrane, with STEM tomography revealing the high connectivity and nontortuous pore structure in three dimensions. The diffusion-limited infiltration and growth of Al_2O_3 precursors in the PMMA block resulted in a gradient in Al_2O_3 content through depth, with larger Al_2O_3 content at the top versus the bottom and hence an increase in pore size from top to bottom of the membrane, as evident from the STEM tomography. This nonhomogeneous depth profile is considered ideal for separation applications.

Combining the thin BCP-templated AlO_x membrane with supporting AAO membrane resulted in hierarchical membrane that was used for separating similar sized proteins. The ultrathin AlO_x nanostructure and the narrowly distributed pore size enabled the hierarchical membrane to separate proteins with both high flux and high selectivity. The processes and membrane fabrication approach developed in this research provide a potential new route for making isoporous metal-oxide membranes. We envision this route as a new platform for advanced and multifunctional membranes that would exhibit high separation selectivity, antifouling behavior, and photocatalytic activity.

4. Experimental Section

Materials: Cylinder-forming PS-*b*-PMMA (C2050, $M_n = 20.2\text{-}b\text{-}50.5$ kg·mol⁻¹, polydispersity index PDI = 1.07) was purchased from Polymer Source, Inc. Poly(acrylic acid) sodium salt solution ($M_w \approx 15\,000$ g·mol⁻¹, 35% mass fraction in water) was purchased from Sigma-Aldrich and used as received. Poly(styrene-*r*-methyl methacrylate-*r*-glycidyl methacrylate) (P(S-*r*-MMA-*r*-GMA)) containing ≈ 4 mol% of glycidyl methacrylate was synthesized by reversible addition fragmentation chain transfer polymerization with styrene mole fractions from 21% to 85% (denoted as 21S to 85S) determined by ¹H nuclear magnetic resonance spectroscopy. Anodic aluminum oxide membranes (Anopore) were purchased from Sigma-Aldrich (20 and 100 nm pore size membranes with 60 μm thickness). Bovine serum albumin (66 kDa) and bovine hemoglobin (65 kDa) were purchased from Sigma-Aldrich, and used as received. The buffer powder for phosphate buffered saline was purchased from Sigma-Aldrich (catalog no. P3563). The pH values of the buffer solutions were tuned to 4.7 and 7.0 by adding a small amount of HCl or NaOH solution.

Sample Preparation: Silicon wafers were cleaned in a piranha solution (3:7 volumetric ratio of concentrated sulfuric acid and 30 wt% hydrogen peroxide solution) at 130 °C for 30 min and rinsed with deionized water prior to use. PS-*r*-PMMA-modified substrates were prepared by spin coating 1 wt% of 21S to 85S in toluene solution onto the cleaned Si wafer at 4000 rpm for 1 min, followed by annealing at 250 °C for 30 min under a nitrogen atmosphere to be fully crosslinked. C2050 films with thickness ranging from 22 to 401 nm were deposited from chlorobenzene solutions with concentrations of 1–8 wt% on the PS-*r*-PMMA-modified substrates. Samples were annealed at 190–270 °C for 30 min to 3 h under a nitrogen atmosphere. Al_2O_3 SIS was performed in Arrandine Gemstar ALD using alternating exposures to TMA and deionized H₂O at 95 °C in semistatic mode. N₂ gas flow was used as purge and carrier gas. The base pressure of the reactor was 50 mTorr before introducing the precursors. During each setting exposure period, the TMA valve was opened for 1 s, after which the valve was closed and the samples were exposed for 10 min, and then pure N₂ gas was flowed through the chamber at 200 sccm for 5 min to purge any unreacted precursor. A same exposure/purge process was used for the H₂O precursor to complete one SIS cycle. The long exposure time was chosen to ensure the precursors could diffuse through the entire thickness of the film. The SIS cycle number was varied between 2 and 5. The polymers were etched with O₂ reactive ion etching (RIE) using Oxford Plasma-Pro NGP80. The samples were etched at 50 W radio frequency power for 5 min to make sure polymers were removed thoroughly. Film thickness was measured using an alpha-SE ellipsometer.

Membrane Fabrication: Silicon wafers were piranha cleaned with same procedure. About 100 nm thick water soluble sacrifice layers were prepared by spin coating 5 wt% PAA-Na in water at 4000 rpm for 90 s. 63S was spin-cast from a 1 wt% toluene solution and followed by annealing at 250 °C for 30 min under a nitrogen atmosphere to function as surface neutral layer. C2050 films with thickness of 141 nm were spin-cast from chlorobenzene solutions with concentrations of 4 wt% on the silicon-PAA-mat substrates. Samples were annealed at 270 °C for 3 h under a nitrogen atmosphere. The BCP film and mat were floated using deionized water and transferred onto the commercial AAO supporting membrane, followed by SIS and O₂ RIE as previously described. While the SIS process results in growth of Al_2O_3 also inside the polymer mat,^[30] this nonstructured thin layer is not mechanically stable to be a stand-alone layer and porosity is achieved without breakthrough Al_2O_3 etch.

For STEM imaging samples, the BCP film and mat were floated and collected with a silicon nitride supporting film (200 μm silicon frame, 30 nm silicon nitride supporting film).^[33,48,56] The same SIS and etching recipes were applied to TEM samples.

Scanning Electron Microscopy: A Carl Zeiss Merlin field-emission scanning electronic microscopy was used to investigate the surface morphology with an acceleration voltage of 1 keV and a typical working distance of 3 mm.

Transmission Electron Microscopy: STEM imaging and tomography were performed using a field-emission gun TEM operated at 200 kV, and camera length of 300 mm. For tomography, a series of STEM images were acquired at tilt angles ranging from -68° to $+68^\circ$ at angular interval of 3° from -54° to $+54^\circ$, and at angular interval of 2° from $+54^\circ$ to $+68^\circ$ and from -54° to -68° . The tilt series of the STEM images (51 projections) were aligned with Inspect 3D software using naturally occurring defects in the film. Reconstruction was performed using simultaneous iterative reconstruction technique algorithm applied through the same software. Segmentation (thresholding) of the reconstructed volume was performed manually using ImageJ to define the alumina domains for surface rendering. Visualization of the segmented volume was performed using Amira software.

Image Analysis of Pore Size: Pore size analysis was performed using watershed segmentation algorithm implemented in a python script. Pore diameter was measured as the diameter of a circle with the same area as the segmented pore.

GISAXS: GISAXS measurements were performed at beamline 8-ID-E of the Advanced Photon Source at the Argonne National Laboratory. The X-ray energy was 7.35 keV, the wavelength was 1.69 nm, and the sample to detector distance was 1.30 m. The exposure time to collect each scattering measurement was 1 s. Sets of 30 scattering measurements were collected and integrated to produce each 2D scattering profile.

Protein Transport and Separation: Protein separation was probed in a custom-made U-shaped diffusion cell. Membranes were sandwiched between two glass slides with a hole and two rubber O-rings, and clamped between glass fittings. The effective permeation area of the all membranes was 0.45 cm^2 . Fifteen milliliters of a 0.01 M buffer solutions were placed into the source (including a mixture of $25 \times 10^{-6} \text{ M}$ BSA and $25 \times 10^{-6} \text{ M}$ BHB) and sink chambers. The value of the electrical double layer thickness is given by

$$\lambda_D = (8\pi n_0 \lambda_B)^{-1/2} \quad (1)$$

where the ion density n_0 is ≈ 0.006 for 0.01 M buffer solutions and λ_B is $\approx 0.7 \text{ nm}$ in water.^[21,53] Both compartments were stirred vigorously with magnetic stirrers to ensure homogenic solutions. One milliliter was taken every 60 min from both the sink and the source sides, and the solute concentrations in the sink side were quantified by UV-visible spectroscopy (Agilent 8453), using the absorption band at 278 nm for BSA and at 408 nm for BHB.

Supporting Information

Supporting Information is available from the Wiley Online Library or from the author.

Acknowledgements

C.Z. and T.S.-P. contributed equally to this work. This work was supported by the U.S. Department of Energy, Basic Energy Sciences, Materials Sciences and Engineering Division. This research used resources at the Center for Nanoscale Materials and the Advanced Photon Source, both U.S. Department of Energy Office of Science user facilities operated by Argonne National Laboratory under Contract No. DE-AC02-06CH11357. The authors are grateful for the support at the Searle Cleanroom in the University of Chicago. T.S.-P. is a Horev Fellow, supported by the Taub Foundation and an Azrieli Fellow, supported by the Azrieli Foundation.

Conflict of Interest

The authors declare no conflict of interest.

Keywords

block copolymers, molecular separation, nanoporous alumina membrane, self-assembly, sequential infiltration synthesis

Received: April 3, 2017

Revised: May 26, 2017

Published online:

- [1] C. Dekker, *Nat. Nanotechnol.* **2007**, *2*, 209.
- [2] E. A. Jackson, M. A. Hillmyer, *ACS Nano* **2010**, *4*, 3548.
- [3] J. P. Fu, P. Mao, J. Han, *Trends Biotechnol.* **2008**, *26*, 311.
- [4] S. P. Adiga, C. M. Jin, L. A. Curtiss, N. A. Monteiro-Riviere, R. J. Narayan, *Wiley Interdiscip. Rev.: Nanomed. Nanobiotechnol.* **2009**, *1*, 568.
- [5] S. Majd, E. C. Yusko, Y. N. Billeh, M. X. Macrae, J. Yang, M. Mayer, *Curr. Opin. Biotechnol.* **2010**, *21*, 439.
- [6] S. P. Adiga, L. A. Curtiss, J. W. Elam, M. J. Pellin, C.-C. Shih, C.-M. Shih, S.-J. Lin, Y.-Y. Su, S. D. Gittard, J. Zhang, R. J. Narayan, *JOM* **2008**, *60*, 26.
- [7] M. J. Kim, M. Wanunu, D. C. Bell, A. Meller, *Adv. Mater.* **2006**, *18*, 3149.
- [8] S.-W. Nam, M. J. Rooks, K.-B. Kim, S. M. Rosnagel, *Nano Lett.* **2009**, *9*, 2044.
- [9] C. C. Striemer, T. R. Gaborski, J. L. McGrath, P. M. Fauchet, *Nature* **2007**, *445*, 749.
- [10] A. Lee, J. W. Elam, S. B. Darling, *Environ. Sci.: Water Res. Technol.* **2016**, *2*, 17.
- [11] G. Singh, S. Batra, R. Zhang, H. Y. Yuan, K. G. Yager, M. Cakmak, B. Berry, A. Karim, *ACS Nano* **2013**, *7*, 5291.
- [12] S. Rangou, K. Buhr, V. Filiz, J. I. Clodt, B. Lademann, J. Hahn, A. Jung, V. Abetz, *J. Membr. Sci.* **2014**, *451*, 266.
- [13] F. S. Bates, G. H. Fredrickson, *Annu. Rev. Phys. Chem.* **1990**, *41*, 525.
- [14] S. Y. Yang, J. Park, J. Yoon, M. Ree, S. K. Jang, J. K. Kim, *Adv. Funct. Mater.* **2008**, *18*, 1371.
- [15] S. Y. Yang, I. Ryu, H. Y. Kim, J. K. Kim, S. K. Jang, T. P. Russell, *Adv. Mater.* **2006**, *18*, 709.
- [16] W. A. Phillip, B. O'neill, M. Rodwogin, M. A. Hillmyer, E. L. Cussler, *ACS Appl. Mater. Interfaces* **2010**, *2*, 847.
- [17] K. V. Peinemann, V. Abetz, P. F. W. Simon, *Nat. Mater.* **2007**, *6*, 992.
- [18] R. M. Dorin, H. Sai, U. Wiesner, *Chem. Mater.* **2014**, *26*, 339.
- [19] S. Y. Yang, J. A. Yang, E. S. Kim, G. Jeon, E. J. Oh, K. Y. Choi, S. K. Hahn, J. K. Kim, *ACS Nano* **2010**, *4*, 3817.
- [20] M. A. Hillmyer, *Adv. Polym. Sci.* **2005**, *190*, 137.
- [21] X. Y. Qiu, H. Z. Yu, M. Karunakaran, N. Pradeep, S. P. Nunes, K. V. Peinemann, *ACS Nano* **2013**, *7*, 768.
- [22] B. Nandan, B. K. Kuila, M. Stamm, *Eur. Polym. J.* **2011**, *47*, 584.
- [23] C.-Y. Nam, A. Stein, K. Kisslinger, C. T. Black, *Appl. Phys. Lett.* **2015**, *107*, 203106.
- [24] C. Y. Nam, A. Stein, K. Kisslinger, *J. Vac. Sci. Technol., B: Nanotechnol. Microelectron.: Mater., Process., Meas., Phenom.* **2015**, *33*, 06F201.
- [25] Q. Peng, Y.-C. Tseng, S. B. Darling, J. W. Elam, *Adv. Mater.* **2010**, *22*, 5129.
- [26] Q. Peng, Y.-C. Tseng, S. B. Darling, J. W. Elam, *ACS Nano* **2011**, *5*, 4600.
- [27] C. Cummins, T. Ghoshal, J. D. Holmes, M. A. Morris, *Adv. Mater.* **2016**, *28*, 5586.
- [28] J. Kamcev, D. S. Germack, D. Nykpanchuk, R. B. Grubbs, C. Y. Nam, C. T. Black, *ACS Nano* **2013**, *7*, 339.
- [29] Y. C. Tseng, A. U. Mane, J. W. Elam, S. B. Darling, *Adv. Mater.* **2012**, *24*, 2608.
- [30] Y.-C. Tseng, Q. Peng, L. E. Ocola, J. W. Elam, S. B. Darling, *J. Phys. Chem. C* **2011**, *115*, 17725.

- [31] Y. C. Tseng, Q. Peng, L. E. Ocola, D. A. Czaplewski, J. W. Elam, S. B. Darling, *J. Mater. Chem.* **2011**, *21*, 11722.
- [32] R. Ruiz, L. Wan, J. Lille, K. C. Patel, E. Dobisz, D. E. Johnston, K. Kisslinger, C. T. Black, *J. Vac. Sci. Technol., B: Nanotechnol. Microelectron.: Mater., Process., Meas., Phenom.* **2012**, *30*, 06F202.
- [33] T. Segal-Peretz, J. Winterstein, M. Doxastakis, A. Ramirez-Hernandez, M. Biswas, J. X. Ren, H. S. Suh, S. B. Darling, J. A. Liddle, J. W. Elam, J. J. de Pablo, N. J. Zaluzec, P. F. Nealey, *ACS Nano* **2015**, *9*, 5333.
- [34] S. Ham, C. Shin, E. Kim, D. Y. Ryu, U. Jeong, T. P. Russell, C. J. Hawker, *Macromolecules* **2008**, *41*, 6431.
- [35] W. Gu, S. W. Hong, T. P. Russell, *ACS Nano* **2012**, *6*, 10250.
- [36] E. Han, K. O. Stuen, M. Leolukman, C. C. Liu, P. F. Nealey, P. Gopalan, *Macromolecules* **2009**, *42*, 4896.
- [37] C. T. Black, K. W. Guarini, *J. Polym. Sci., Part A: Polym. Chem.* **2004**, *42*, 1970.
- [38] S. X. Ji, C. C. Liu, W. Liao, A. L. Fenske, G. S. W. Craig, P. F. Nealey, *Macromolecules* **2011**, *44*, 4291.
- [39] E. Han, K. O. Stuen, Y. H. La, P. F. Nealey, P. Gopalan, *Macromolecules* **2008**, *41*, 9090.
- [40] C.-C. Liu, E. Han, M. S. Onses, C. J. Thode, S. Ji, P. Gopalan, P. F. Nealey, *Macromolecules* **2011**, *44*, 1876.
- [41] P. A. R. Delgadillo, R. Gronheid, C. J. Thode, H. Wu, Y. Cao, M. Neisser, M. Somervell, K. Nafus, P. F. Nealey, *J. Micro/Nanolithogr., MEMS, MOEMS* **2012**, *11*, 31302.
- [42] A. M. Welander, G. S. W. Craig, Y. Tada, H. Yoshida, P. F. Nealey, *Macromolecules* **2013**, *46*, 3915.
- [43] H. S. Suh, H. Kang, P. F. Nealey, K. Char, *Macromolecules* **2010**, *43*, 4744.
- [44] W. J. Durand, M. C. Carlson, M. J. Maher, G. Blachut, L. J. Santos, S. Tein, V. Ganesan, C. J. Ellison, C. G. Willson, *Macromolecules* **2016**, *49*, 308.
- [45] P. Busch, M. Rauscher, J. F. Moulin, P. Muller-Buschbaum, *J. Appl. Crystallogr.* **2011**, *44*, 370.
- [46] T. Vu, N. Mahadevapuram, G. M. Perera, G. E. Stein, *Macromolecules* **2011**, *44*, 6121.
- [47] A. Singh, W. Knaepen, S. Sayan, Z. el Otell, B. T. Chan, J. W. Maes, R. Gronheid, *Proc. SPIE* **2015**, *9425*, 94250N.
- [48] J. Ren, L. E. Ocola, R. Divan, D. A. Czaplewski, T. Segal-Peretz, S. Xiong, R. J. Kline, C. G. Arges, P. F. Nealey, *Nanotechnology* **2016**, *27*, 435303.
- [49] M. Biswas, J. A. Libera, S. B. Darling, J. W. Elam, *J. Phys. Chem. C* **2015**, *119*, 14585.
- [50] M. Biswas, J. A. Libera, S. B. Darling, J. W. Elam, *Chem. Mater.* **2014**, *26*, 6135.
- [51] N. Ileri, R. Faller, A. Palazoglu, S. E. Letant, J. W. Tringe, P. Stroeve, *Phys. Chem. Chem. Phys.* **2013**, *15*, 965.
- [52] H. U. Osmanbeyoglu, T. B. Hur, H. K. Kim, *J. Membr. Sci.* **2009**, *343*, 1.
- [53] T. M. Squires, S. R. Quake, *Rev. Mod. Phys.* **2005**, *77*, 977.
- [54] P. Stroeve, M. Rahman, L. D. Naidu, G. Chu, M. Mahmoudi, P. Ramirez, S. Mafe, *Phys. Chem. Chem. Phys.* **2014**, *16*, 21570.
- [55] E. Dickey, W. A. Barrow, *J. Vac. Sci. Technol., A* **2012**, *30*, 21502.
- [56] T. Segal-Peretz, J. Winterstein, M. Biswas, J. A. Liddle, J. W. Elam, N. J. Zaluzec, P. F. Nealey, *Microsc. Microanal.* **2015**, *21*, 611.